The effects of tensile and compressive dwells on creep-fatigue behavior and fracture mechanism in welded joint of P92 steel

Yuxuan Song[1,2] , Yi Ma[1,*], Haofeng Chen[3], Zhibo He[1,2],

Hu Chen[5], Taihua Zhang[6] and Zengliang Gao[1,2,4 *]

1. College of Mechanical Engineering, Zhejiang University of Technology, Hangzhou, 310014.

2. Institute of Process Equipment and Control Engineering, College of Mechanical Engineering, Zhejiang University of Technology, Hangzhou, 310014.

3. Department of Mechanical and Aerospace Engineering, University of Strathclyde, Glasgow, UK, G1 1XJ.

4. Engineering Research Center of Process Equipment and Re-manufacturing, Ministry of Education, Hangzhou, China.

5. Ningbo Special Equipment Inspection and Research Institute, Ningbo, 315000.

6. Institute of Solid Mechanics, Beihang University, Beijing, 100191，PR China.

* Corresponding author E-mail: may@zjut.edu.cn; zlgao@zjut.edu.cn

Abstract: The creep-fatigue interactions on the long-term service damage of P92 welded joint were investigated on the tensile and compressive holdings with a series of applied strains, respectively. The local mechanical properties including hardness, elastic modulus and creep resistance of welded joint were uncovered using nanoindentation. The features of fracture morphology and internal defects after CF tests were studied by scanning electron microscope. Based on the characteristic of microstructural evolution and the variation in local mechanical properties, holding type effects of creep-fatigue interaction on the local creep behavior and fracture mechanism of the welds were systematically investigated.

  Key Words: P92 steel welded joint; Creep-fatigue interaction; Nanoindentation; Creep; Fracture

Nomenclature

Parent plate	PP
Heat affected zone	HAZ
Fine-grained heat affected zone	FGHAZ
Coarse-grained heat affected zone	CGHAZ
Weld metal	WM
Creep-fatigue	CF
Scanning electron microscope	SEM
Finite element	FE
Gas tungsten arc welding	GTAW
Submerged arc welding	SAW
Electro-discharge machining	EDM
Continuous stiffness measurement	CSM
Tensile holding	TH
Compressive holding	CH
Prior austenite grain	PAG
Prior austenite grain boundary	PAGB
Strain rate sensitivity	SRS

1. Introduction

Welding technologies are widely used for construction of modern fossil fuel and nuclear power plants [1-3]. Welded joints are a critical part of the welded structure and typically have strongly graded microstructure, transitioning from PP through the heat affected zone (HAZ, which can be divided into fine-grained and coarse-grained regions) to the fusion zone, or WM. The heterogeneity in microstructure and local mechanical properties of the welded joint leads to high-temperature instability of the welded structure [4-6]. In power plants, welded joints experience CF loading due to frequent start-ups and shut-downs coupled with high temperature operation [7-9]. Under high-temperature CF loading, several damage processes occur simultaneously: softening under cyclic loading, accumulation of creep damage during holding periods (dwell) and a contribution from creep-fatigue [8-10]. This is a complex interaction that can result in premature failure of the welded joints, particularly at operating temperatures beyond 600°C for steels [11-13]. To assist in an improved evaluation of the remaining life of existing power plant, it is therefore essential to understand local creep behavior and the fracture mechanisms in welded joints after they have experienced prior CF loading.

In recent decades, investigations on the remnant creep properties of homogeneous materials after prior fatigue or CF loading have attracted significant attention [14-18]. For example, Sarker et al [14] performed conventional creep tests after prior fatigue loading, and found that the reduction in remaining creep life was related to the number of prior fatigue cycles. Zhang et al [18] studied the remnant tensile strength and creep behavior of P92 steel after prior CF and concluded that the reduction in remnant creep resistance was commonly caused by the growth of martensitic laths. Other work has found that mode of holding period, i.e. tensile or compressive, strongly affects the creep-fatigue resistance of steels [19, 20]. Fournier et al [19], in work on P91 steel, found that periods of compressive dwell were more deleterious than tensile dwell and that this phenomenon was more pronounced at low strain ranges. Gao et al [20] found that intergranular long cracks were formed under tensile stresses, while transgranular short cracks were occurred under compressive stresses for 316 stainless steel. However, there are still only a limited number of investigations that have focused on the remnant creep properties of homogeneous materials after prior CF loading with tensile and compressive dwell periods of differing length. Since the CG and FG HAZ microstructures are narrow (1-2 mm) their mechanical heterogeneity cannot be precisely measured using conventional uniaxial tension, compression or bending tests. In this scenario, nanoindentation dwell tests have become a popular and effective method to study creep deformation in numerous materials, particularly high entropy alloys, e.g. metallic glasses, where the work uses small samples, often with surface coatings and a strongly heterogeneous structure [21-25]. Nanoindentation offers the advantages of ultra-high

sensitivity to displacement and load and provides a high shear-compressive stress region beneath the indenter, allowing creep deformation to be clearly observed at ambient temperatures even for materials with a high-melting point [21-23]. The local creep behavior of the HAZ regions in welded joints of SA508 Gr3 steel has also been studied using nanoindentation [26]. Under long-term high-temperature creep flow, voids have been observed to form at grain boundaries in the HAZ, with their density being significantly higher in the FG HAZ and also increasing with creep time [18, 27]. Creep voids act as local stress concentration sites during periods of dwell loading and promote further creep deformation and voiding, eventually leading to the initiation of small cracks. Creep during nanoindentation is induced from the high-stress region beneath the indenter and can therefore be used to investigate the local creep resistance of alloys that have experienced previous creep or CF damage.

Furthermore, under CF loading, crack propagation in fatigue is closely related to the local creep resistance near the crack tip [28-30], and accumulated creep damage near the fatigue crack tip would further increase the fatigue crack propagation rate [28-30]. To date, creep damage has been more widely investigated via FE stress analysis rather than by using experimental methods such as mechanical testing. Since creep resistance near the crack is difficult to measure the fracture mechanisms of welded joints experiencing CF rupture have not been extensively studied. However, nanoindentation techniques now offer the opportunity to measure the local creep resistance and other mechanical properties near the fractured edge of specimens that have undergone CF rupture. Investigation of the mechanical properties and microstructural evolution near the fracture surface can elucidate the mechanisms involved in fracture of a welded joint under CF loading. Our previous work [28-31]on P92 steel investigated the local creep behavior of a welded joint under CF loading. However, the effect of the type of dwell period, i.e. whether it is tensile or compressive, on the creep behavior of welded joints is still an open question.

ASTM A355 P92 steel is 9Cr-2Mo steel that is widely used as a new generation creep strength-enhanced ferritic steel for steam pipes and super-header components in nuclear and fossil-fuel power plants [31]. The work reported in the current paper focuses on the local creep behavior and fracture mechanism of P92 steel welds after prior loading with tensile and compressive dwell periods. Relying on nanoindentation, hardness, elastic modulus and creep deformation were individually measured near the fractured edge (Crack region), as well as in the PP, FGHAZ, CGHAZ and WM regions of specimens after CF loading with tensile or compressive dwell at low strain amplitudes. The fracture surface features at the welded joint under CF loading with long-term tensile or compressive dwell were characterized using SEM. Thus the present work systematically investigates local creep behavior and fracture mechanisms in P92 steel welded joints after different loading sequences and their correlation with the local microstructural evolution.

2. Materials and experimental procedures

2.1 Materials

This study focuses on studying welded joints in a commercial Chinese Grade P92 steel pipe, using sections 80 mm thick, diameter 840 mm and length 600 mm. Two pipe sections were welded together using either GTAW or SAW. The welded pipe was then annealed at 760°C for 2 hours followed by air cooling. The completed welds were subjected to nondestructive inspection to ensure that the joint met the specified industrial requirements. The typical chemical composition range for P92 steel along with the specific compositions of the alloy and welding consumable are provided in Table 1.

Table 1 Chemical composition of P92 steel and the welding consumable (wt.%)

Element	C	Si	Mn	Ni	Cr	Mo	P	S	N	W	B	Nb
Specified	0.07-0.13	<0.50	0.30-0.60	<0.40	8.50-9.50	0.30-0.60	<0.02	<0.01	0.03-0.07	1.50-2.00	10-60ppm	0.04-0.09
P92 pipe	0.106	0.235	0.361	0.108	9.220	0.374	0.017	0.008	0.061	1.61	25ppm	0.049
P92 wire	0.095	0.150	0.610	0.680	8.360	0.940	0.011	0.007	0.041	1.58	55ppm	0.078

The welded joint was polished and etched using a mixture comprising 92 ml water, 4 ml hydrofluoric acid and 4 ml nitric acid. Etched microstructures of the PP, FGHAZ, CGHAZ and WM were examined with confocal laser scanning microscopy (CLSM, OLYMPUS OLS4500), and typical regions are shown in Figures 1(a) - 1(d). Tempered martensitic laths were seen to exist in the PAGs. Fine PAGs were also observed in the PP and FGHAZ regions, while coarser PAGs were seen in the CGHAZ and WM regions.
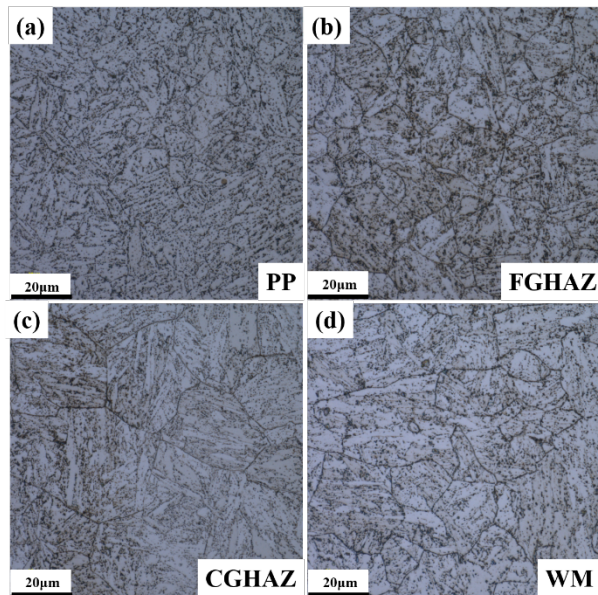
Figure 1.   Microstructures of the (a) PP, (b) FGHAZ, (c) FGHAZ, and (d) WM regions in the as-welded P92 welded joint [28].

2.2 Creep-fatigue experiments

Using EDM, specimens were cut through the pipe thickness, as shown in Figure 2(a) so as to sample all four regions in a welded pipe joint. In this study, the specimens were cut from the same position of the welded joint to ensure the similar initial mechanical properties for each specimen. Figure 2(b) shows the finished shape of the machined specimens before testing. CF experiments were performed in a high-temperature electronic creep-fatigue testing machine (RPL 300, and the maximum loading capacity is 100 KN) at 650°C. Symmetric trapezoidal waveforms were used in the CF tests, and a matrix of test parameters used in the CF experiments is given in Table 2. The strain rate was kept constant at 0.001 s^{-1}, while the dwell time and strain amplitudes were different for each specimen (Table 2). The gauge length change in the specimen was measured using an extensometer (Epsilon, the gauge length is 25 mm and the resolution is 0.001 mm) during the CF tests, with a data acquisition frequency of 10 Hz. All specimens were held for at least 30 minutes at 650°C before the CF experiments started to ensure a uniform temperature in them. Temperature variation during testing was maintained at ＜±1°C using three S-type thermocouples, which were fixed to the top, middle and bottom of the specimen.
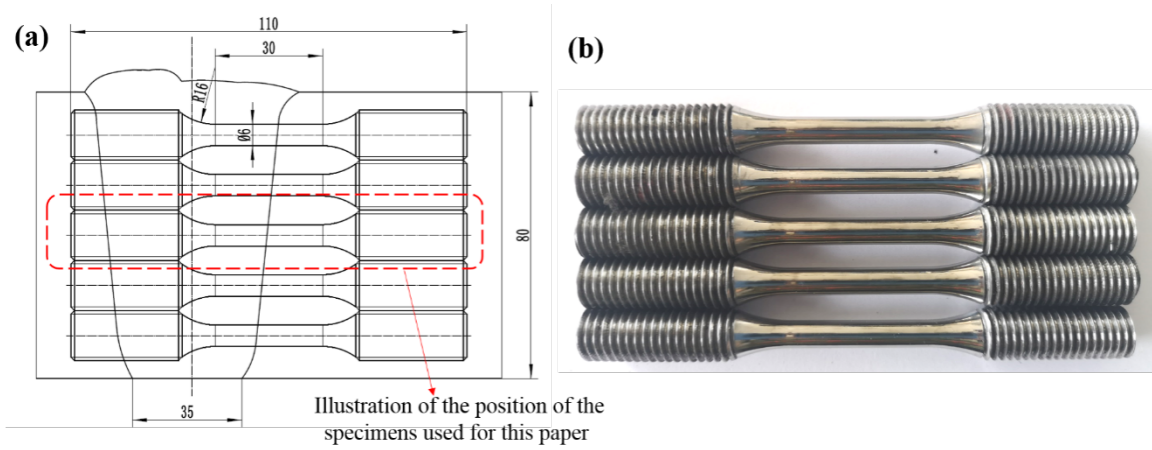
Figure 2 (a) Illustration of the position, relative to the weld, of the CF specimens and of their geometry; (b) The machined specimens.

Table 2 Experimental CF test parameters and test results at 650°C

Specimens	Strain rate (s^{-1})	Strain amplitude (%)	Holding time at tension (s)	Holding time at compression (s)
HBI113	0.001	±0.05	300	30
HBI213	0.001	±0.05	30	300
HBI313	0.001	±0.10	300	30
HBI413	0.001	±0.10	30	300
HCI113	0.001	±0.20	300	30
HCI213	0.001	±0.20	30	300
HCI313	0.001	±0.25	300	30
HCI413	0.001	±0.25	30	300

2.3 Nanoindentation testing

Nanoindentation experiments were conducted on an Agilent Nano Indenter G200 at room temperature. Samples for nanoindentation tests were cut from both as-welded and CF-tested specimens using EDM. All specimens tested included microstructures from the PP, FGHAZ, CGHAZ and WM regions. Taking the distance to the fractured edge as a reference, measurement positions for all the regions were recorded in detail. Prior to nanoindentation, samples were polished to a mirror surface by precise polishing (Nanopoli-100). Diamond abrasive at the average size of 2 μm (8000#) and polyurethane polish pad were adopted. After 60-min polishing, samples were cleaned in the anhydrous alcohol by ultrasonic cleaning. Using a standard Berkovich indenter, the nanohardness and elastic modulus of each region were first measured using the CSM technique at strain rate of 0.05 s^{-1}, and the maximum depth of indentation was 2000 nm. The CSM technique allows measurement

of depth-dependent properties of materials in a single step process. The method involves applying a dynamic load superimposed on the static load during loading. The dynamic part of the load is then used to measure the stiffness which can be further processed to calculate the modulus and hardness of the material.

Subsequently, the constant load-holding method was used to investigate local creep behavior. It is widely accepted that the higher initial holding depth can induce more pronounced local creep displacement for nanoindentation [21-24]. Therefore, nanoindentation creep was measured at the same initial holding depth of 1000 nm. Nanoindentation can be used to measure creep behavior with this method by fitting depth versus time data obtained at constant load to appropriate models of material behavior. Strain rate was constant at 0.05 s^{-1} and the indenter was held for 500 s at a depth of 1000 nm in all tests. To investigate the creep-fatigue fracture mechanism, the hardness, elastic modulus and creep deformation in the fracture edge (named the Crack region) were also measured for the CF-tested specimens under a ±0.25% strain amplitude. To ensure statistical reliability of the nanoindentation data, 12 indentations were made in each microstructural region spaced apart by an interval of > 50 μm. Nanoindentation tests were only commenced once thermal drift had reduced below 0.05 nm/s. Subsequently, after unloading specimens, a thermal drift correction was calibrated at 10% of the maximum applied load. Figures 3(a) and 3(b) show the schematic diagrams of the indentation position in the CF-tested specimens with ±0.25% strain amplitude, together with the schematic diagram of nanoindentation regions.
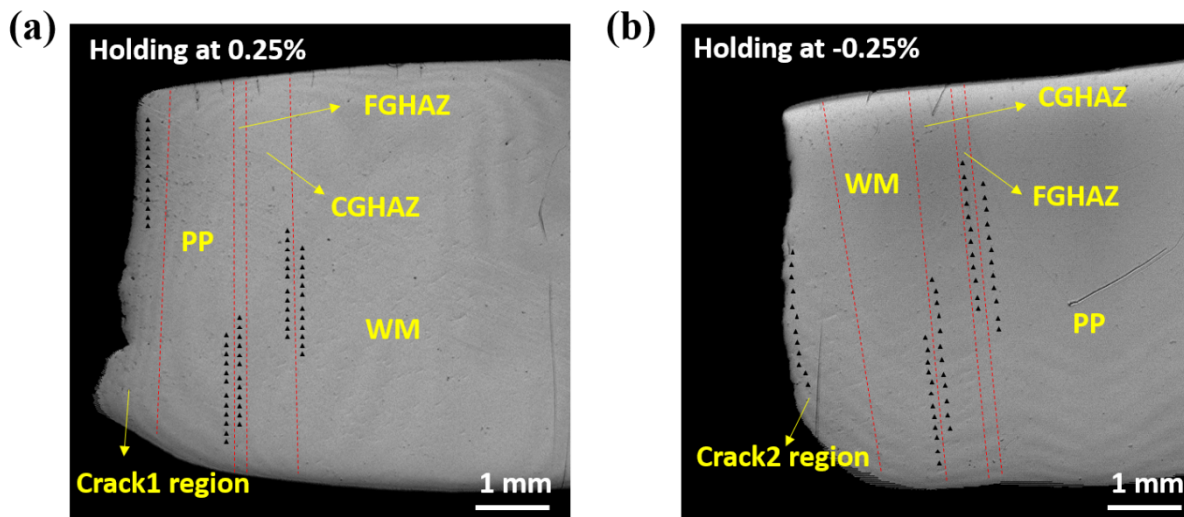

Figure 3 The schematic diagrams of the indentation position for the CF-tested specimens, which were held for 300 s at (a) 0.25% and (b) -0.25% strains.

3. Results

3.1 Microstructural evolution during creep-fatigue

In the following discussion, the specimens subjected to a 300 second period of compressive or tensile dwell are referred to as CH or TH specimens, respectively. The cyclic life of CH specimens are 1473 (±0.05%), 1403(±0.10%), 1123(±0.20%) and 796 (±0.25%), while cyclic life of TH specimens are 3354(±0.05%), 2638(±0.10%), 2611 (±0.20%) and 1488(±0.25%), respectively. Considering the 300 second results, it is clear that the cyclic lives are inversely proportional to the strain amplitudes, as expected. It can also be seen that cyclic lives after a period of compressive dwell are significantly lower than for a tensile dwell period at the same strain amplitude. This reduction in life ranges from 46.5% at a strain amplitude of 0.25% to 56.0% at a strain amplitude of 0.05%, although without demonstrating a consistent trend in the life reduction with the value of strain amplitude. It was also observed that all the specimens fractured in the PP region with the exception of the specimen subject to CH at -0.25% strain amplitude, which fractured in the WM.
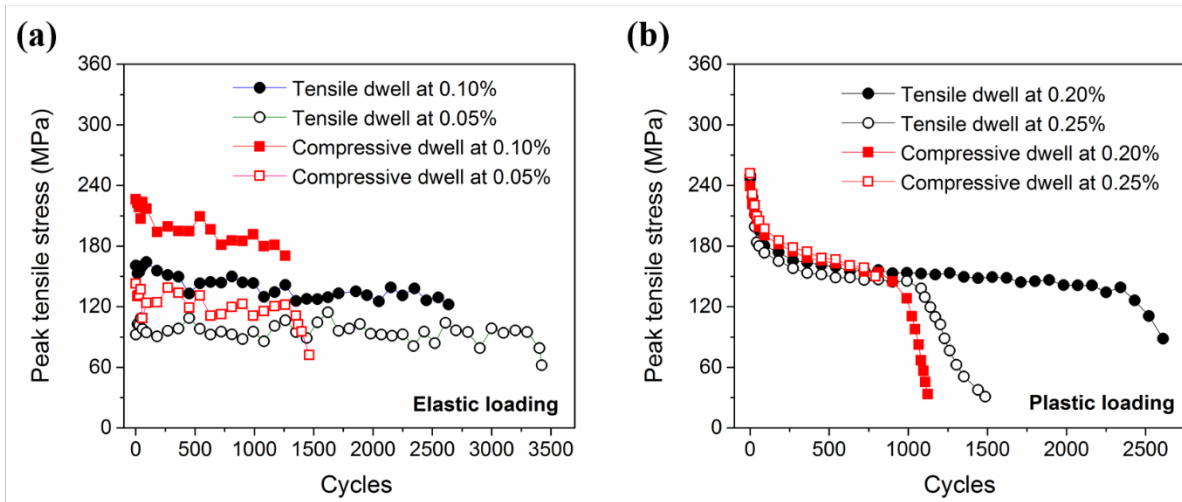

Figure 4 Curves showing the decay in tensile stress during CF testing (a) data for the 0.05% and 0.10% tests, where the decline is primarily due to a change in elastic strain amplitude with life (b) data for the 0.20% and 0.25% tests, where the decline primarily reflects a change in plastic strain amplitude.

Figure 4 shows the change in peak tensile during the CF tests as a function of cyclic life under a 300 s dwell in both tension and compression. In all cases a steady decline through life is observed although larger differences are apparent between CH and TH data at the two lower strain amplitudes (Figure 4a) than for the two higher strain amplitudes (Figure 4b). It is clear in graphs, the cyclic life is longer at a given value of applied strain amplitude when the specimens experience tensile dwell during the test. In the higher strain amplitude data in Figure 4(b), the three stages of creep, representing the influence of three stages in cyclic softening, are more clearly observed, than in the lower amplitude data given in Figure 4(a). The peak tensile stress reduces rapidly reduced in stage 1

from approximately 260 MPa to 155 MPa within the first 400 cycles of loading. The decrease slows during stage 2 and becomes linear over a range of peak tensile stress from approximately 155 MPa to 140 MPa. In the third stage, the peak tensile stress experiences a sharp reduction to final fracture except in the case of the CH specimen with an applied strain amplitude of -0.25%, which fractured in the WM rather than in the PP. In Figure 4(a), however, a larger fluctuation in data is apparent through life, and the three stages of creep are not as clearly defined, being most apparent in the CH test at -0.10% strain amplitude.
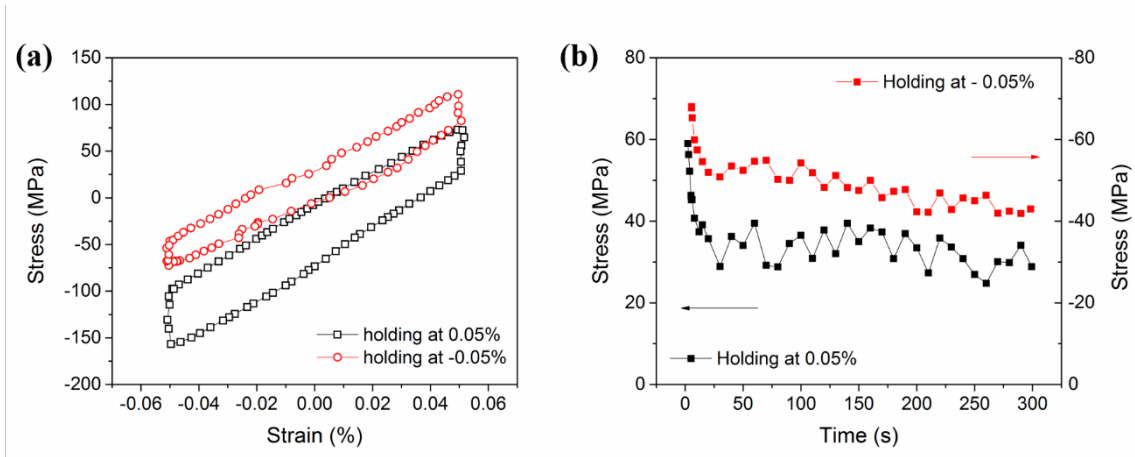
Figure 5(a) Stress-strain hysteresis loops at 50% of the life for the tests at ±0.05% elastic strain amplitude. (b) The stress relaxation observed during the corresponding dwell period of 300 s.

It is widely reported that the stress-strain hysteresis loop of 50% life was an important state to characterize the creep-fatigue interaction [32-34]. Figure 5(a) shows the stress-strain hysteresis loops measured at 50% life (1672th for the tensile- dwell specimen, 736th for the compressive-dwell specimen) for the CF tests conducted at 0.05% elastic strain amplitude. It is observed that the TH specimen subjects to compressive mean stress, while CH specimen experience tensile mean stress. This observation is widely reported by other researchers [35-37]. The tensile mean stress would be generated in the compressive-dwell tests, which could accelerate the creep damage [35-37], so as to reduce cyclic life. Figure 5(b) shows the stress relaxation observed during the holding periods for this same cycle of loading. Stress relaxation during the dwell period can be seen to follow two stages, as generally occurs in creep, namely a rapid initial softening, followed by a stage of stabilized creep. Considering the test with negative dwell, over the period where the peak compressive load was held constant, the stress decreased from -70 MPa to -50 MPa in the initial 30 s, then decreased more slowly from -50 MPa to approximately -42 MPa over the remaining dwell period. For the tensile dwell case, the stress decreased from 60 MPa to approximately 35 MPa in the initial 30 s, then declined slowly to approximately 30 MPa albeit with a significant level of stress fluctuation (≈±5 MPa). For the

specimen that was subjected to dwell with a 30 s holding period at an applied strain amplitude of 0.05%, the stress in the CH specimen reduced from 110 MPa to 50 MPa over the 30 s dwell, while for the TH specimen stress decreased from -160 MPa to -100 MPa during the dwell period. It is therefore clear that the stress relaxation during the 30 s dwell was greater than for the 300 s dwell for both TH and CH tests.
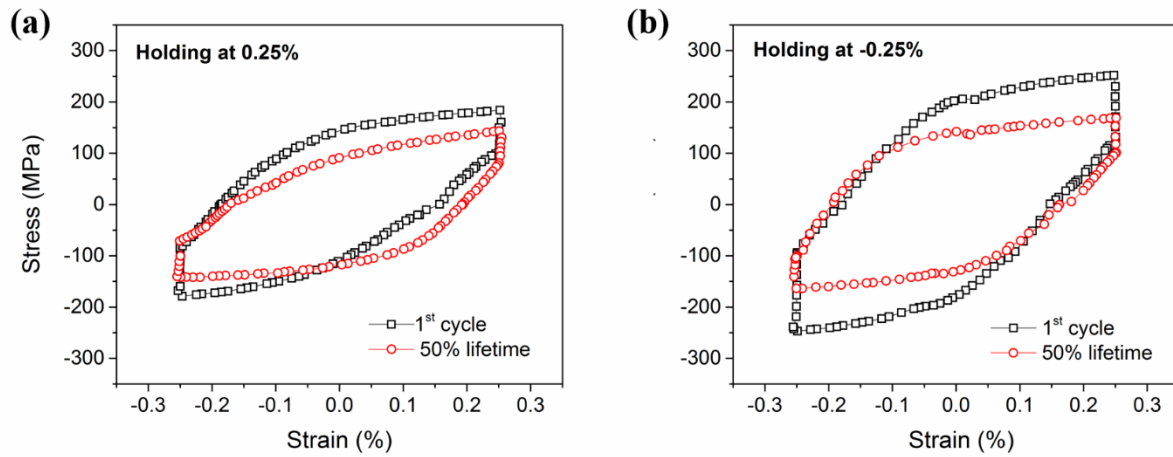

Figure 6 The stress-strain hysteresis loops measured in the first cycle and the cycle equivalent to 50% life with a dwell period of 300 s for the (a) TH (0.25%) and (b) CH (-0.25%) specimens.

Figure 6 shows stress-strain hysteresis loops measured in the CF tests at ±0.25% strain amplitude for the first loading cycle and for the load cycle equivalent to 50% life (700th for the tensile- dwell specimen, 400th for the compressive-dwell specimen) for the TH (Figure 6a) and CH (Figure 6b) tests with a 300 s dwell. In both the TH and CH tests, the peak stress in the first load cycle is higher than in the cycle equivalent to 50% life. It is interesting to note that while the first cycle peak CH stress is higher (≈250 MPa) than in the TH test (≈ 200 MPa), at 50% life the peak stress in both tests is very similar at ≈150 MPa. The different peak stress in the first cycle could result from the slightly different mechanical properties of the across-weld specimens.
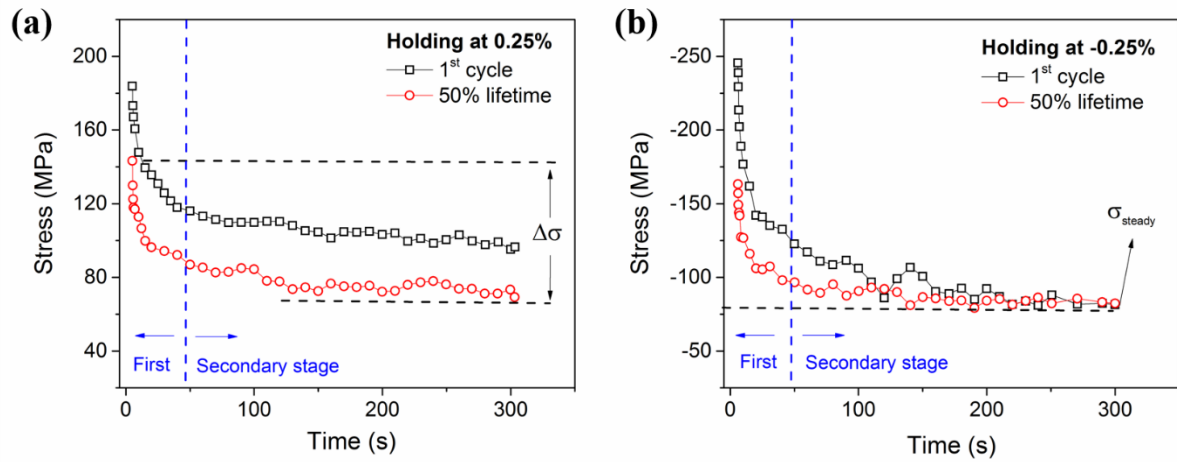
Figure 7 The stress relaxation during the 5-mins holding periods of 1st cycle and 50% lifetimes of the (a) TH (0.25%) and (b) CH (-0.25%) specimens.

Figure 7 gives equivalent data for stress relaxation measured during the 300 s dwell period in the first load cycle and in the cycle equivalent to 50% life for the TH (Figure 7a) and CH (Figure 7b) specimens at an applied strain amplitude of ±0.25%. As was the case at the tests performed with an applied strain of ±0.05% (Figure 5b), two softening stages can be observed. To describe the observed stress relaxation behavior in these tests, two variables are proposed in this study, a parameter that characterizes the initial stress relaxation, $\Delta\sigma$, and a parameter that characterizes the stage 2 steady stress $|\sigma_{steady}|$. A higher value of $\Delta\sigma$ implies an increased stress relaxation in the rapid softening stage of the applied dwell, while $|\sigma_{steady}|$ describes the stress level attained in the stabilized stage. Values of these two parameters are plotted in Figure 8 for two CF tests at ±0.25% strain amplitude, for both the first loading cycle and the cycle at 50% life.
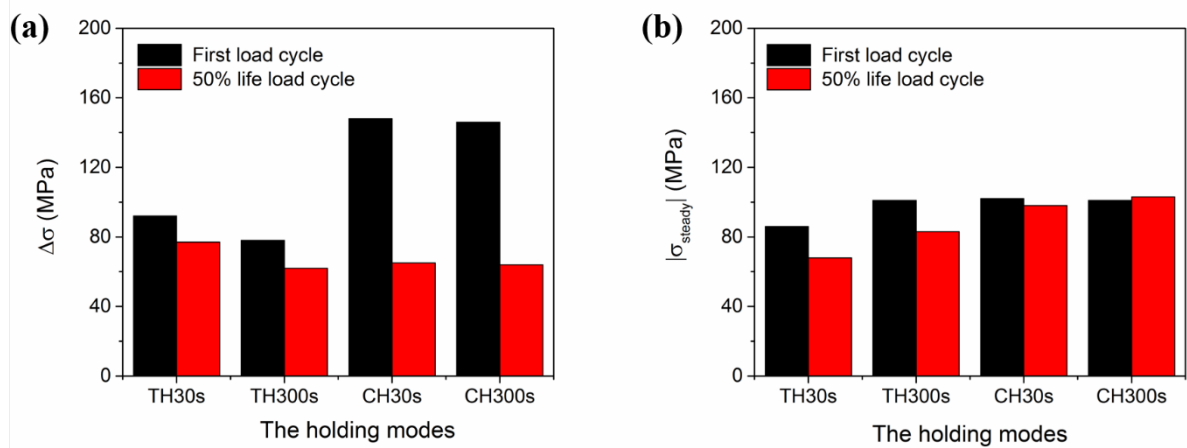

Figure 8 Values of the parameters (a) $\Delta\sigma$ and (b) $|\sigma_{steady}|$ characterizing stress relaxation

during dwell periods at ±0.25% strain for both CH and TH specimens

Figure 8(a) indicates that the initial stress relaxation behavior (Δσ) of 30 s and 300s dwell for rather the TH or CH specimen were all decreased during the CF process. It should be noticed the reduction in Δσ were 19.4% and 25.8% for 30 s and 300 s dwell of the TH specimen, while the corresponding value were 127.7% and 128.2% for 30 s and 300 s dwell of the CH specimen. Figure 8(b) shows the values of $\left|\sigma_{steady}\right|$ of 30 s and 300s dwell for rather the TH or CH specimen. The $\left|\sigma_{steady}\right|$ of both 30 s and 300 s dwells for the CH specimen were higher than the TH specimen. Furthermore, the reduction in $\left|\sigma_{steady}\right|$ were 26.5% and 21.7% for 30 s and 300 s dwell of the TH specimen, while the corresponding value were almost unchanged for both dwells of the CH specimen. Therefore, the $\left|\sigma_{steady}\right|$ for the CH specimen was higher and higher than the TH specimen in both dwells.
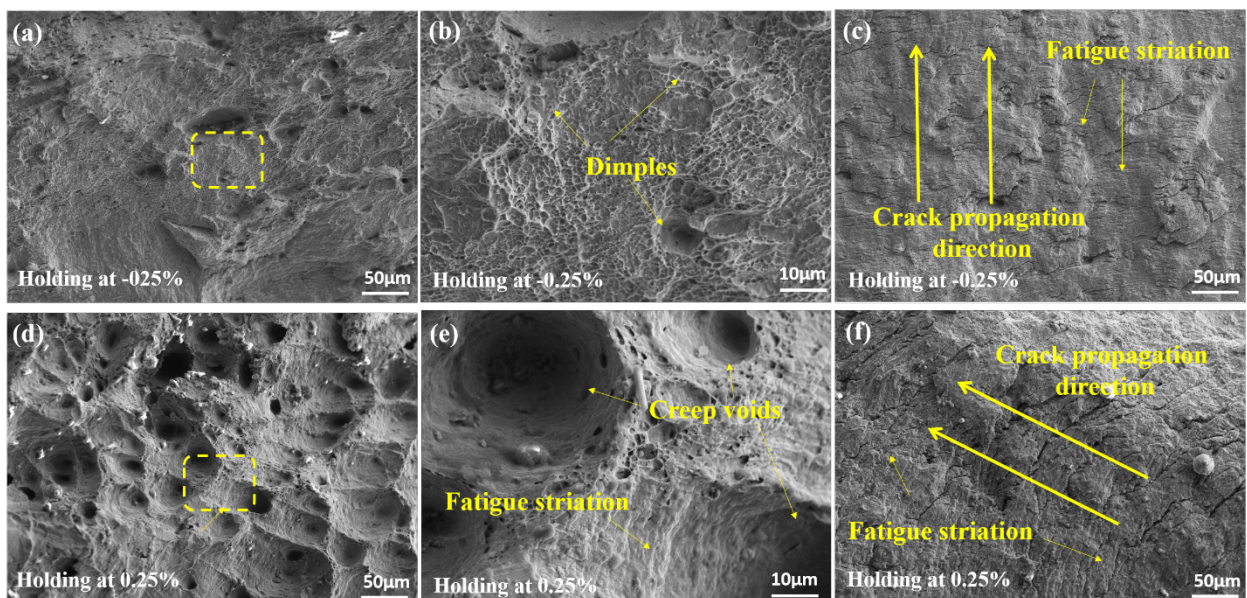

Figure 9 Fracture morphologies of CF specimens subjected to (a), (b) and (c) compressive dwell (CH) at -0.25% for 300 s; (d), (e) and (f) tensile dwell (TH) at -0.25% for 300 s.

The fracture surfaces of the CF specimens tested at an applied strain of ±0.25% were observed using SEM and typical fractographs are shown in Figures 9(a) to 8(f). Figure 9(b) and (e) were the high magnification images of the yellow line surrounded regions in Figure 9(a) and (d), respectively. Figure 9(a) and (b) show that in the CH specimen with a 300 s dwell period and a strain of -0.25%, small dimples (diameter ≈1 μm) were present on the fracture surface and that no creep voids could be observed. Typical fatigue striations were, however, found, as indicated in Figure 9(c). The direction of crack propagation is also shown in the image, marked with yellow arrows. Figures 9(d) to (f) show the morphology of the fracture surface for the TH specimen under equivalent test

conditions. Numerous large creep voids (diameter ≈30 μm) can be seen, as shown in Figure 9(d) and (e). The fatigue striations were observed around the creep voids in Figure 9(c). Figure 9(f) shows that more pronounced fatigue striations were present than was the case for the CH specimen. These observations demonstrate that the fracture mechanism in the welded P92 steel joint reflects the combined effect of creep, fatigue and creep-fatigue interactions.
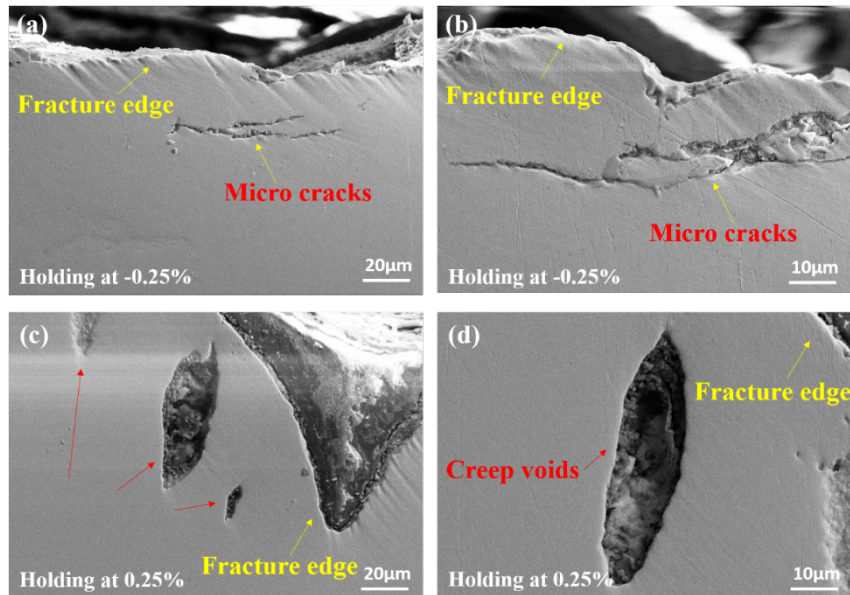

Figure 10 The morphologies near the fracture edge of the specimens subjected to various CF loading (a) and (c) compressive dwell at -0.25%, (c) and (d) tensile dwell at 0.25%.

In order to illustrate crack initiation mechanisms in CH and TH specimens, Figures 10(a) and 10(b) show micrographs of small defects just below the fracture surface of the CH specimen, subject to -0.25% strain and a dwell period of 300 s. Several microcracks were observed with a typical length of ≈60 μm, that were orientated approximately parallel to the fracture surface. Figure 10(c) and (d) show the microdefects seen in the TH specimen subject to 300 s dwell an applied strain of 0.25%. Elliptical creep voids with a diameter up to ≈60 μm) were observed, orientated at approximately 45° to the fracture surface. In fact, this observed regions were the high magnification images for the bottom of the fracture edge in the Figure 3(a). The fracture edge in this regions were almost 45° to the loading direction. Thus the elliptical creep voids were approximately parallel to the loading direction. In all cases, the micro-defects were found within approximately 20-30 μm of the fracture surface. The micrographs in Figure 9 and Figure 10, show that the dominant fracture mechanisms were different between the TH and CH specimens. The existence of numerous, large creep voids suggests that creep damage is dominant in the TH specimen, while fatigue crack initiation appears to be the dominant mechanism in the CH specimen.

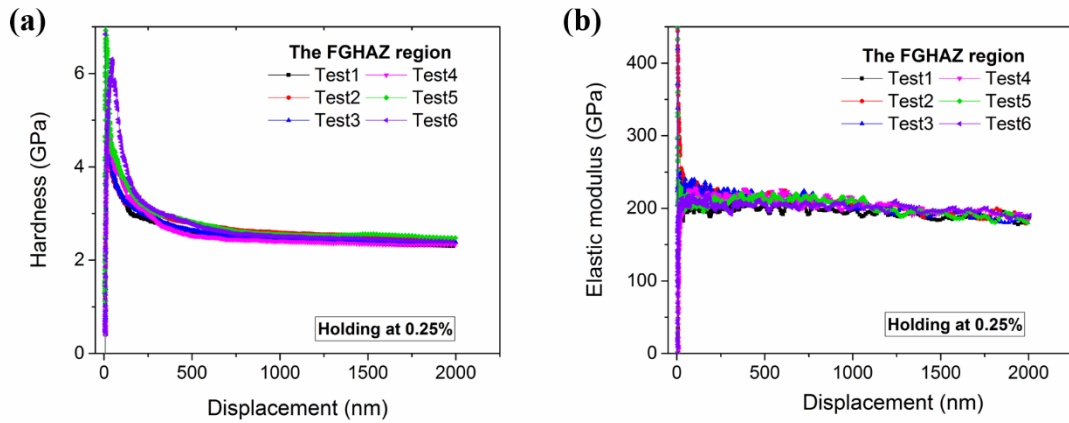## 3.2 Nanoindentation hardness and elastic modulus

Figure 11 the typical (a) Hardness and (b) Elastic modulus as a function of indentation depth, assessed by the CSM technique, in the FGHAZ region of the TH (0.25%) specimen.
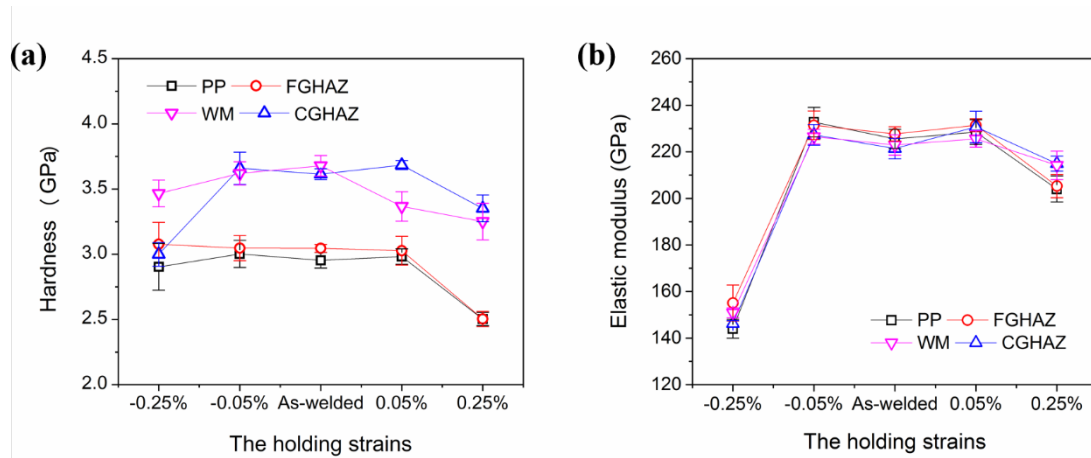

Figure 12(a) Hardness and (b) elastic modulus of the four weld regions assessed by the CSM method, plotted as a function of dwell strain.

Figures 11(a) and 10(b) respectively show the hardness H and elastic modulus E as a function of indentation depth, measured in the FGHAZ region of TH (0.25% strain) specimen. An ISE is clear in the hardness values, evidenced as a sharp decrease in hardness with increasing penetration depth. This effect becomes negligible beyond a penetration depth of ≈300 nm and the hardness reaches a stable value of ≈250 GPa. In contrast, the elastic modulus shows a slight linear decrease with increasing penetration depth. It worth noting that the CSM results show a high level of repeatability in the elastic modulus data from all four weld regions at all the values of dwell strain considered, as shown in Figure 12(b). The hardness data from all four regions, given in Figure 12(a), indicate an influence of microstructural dimension, as the data for the closely linked WM and CGHAZ regions are very similar except at an applied dwell strain of -0.25%, and the data for the adjacent PP and

FGHAZ regions are also very similar at all values of dwell strain. Figure 12 also show that there is a significant effect of the value of the dwell strain on the mechanical properties and that the effect on hardness and elastic modulus becomes much larger at ±0.25% dwell strain. The elastic modulus was fairly constant at ≈225 GPa for as-welded (equivalent to 0% applied strain) and the specimens tested at ±0.05% strain. At an applied dwell strain of ±0.25%, the elastic modulus was reduced to ≈205 GPa in the TH specimen, and ≈150 GPa for the CH specimen. It is likely that the higher strain values induce enhanced creep during the dwell period that results in the reduced hardness and elastic modulus in the four regions of the welded joint in the P92 steel.
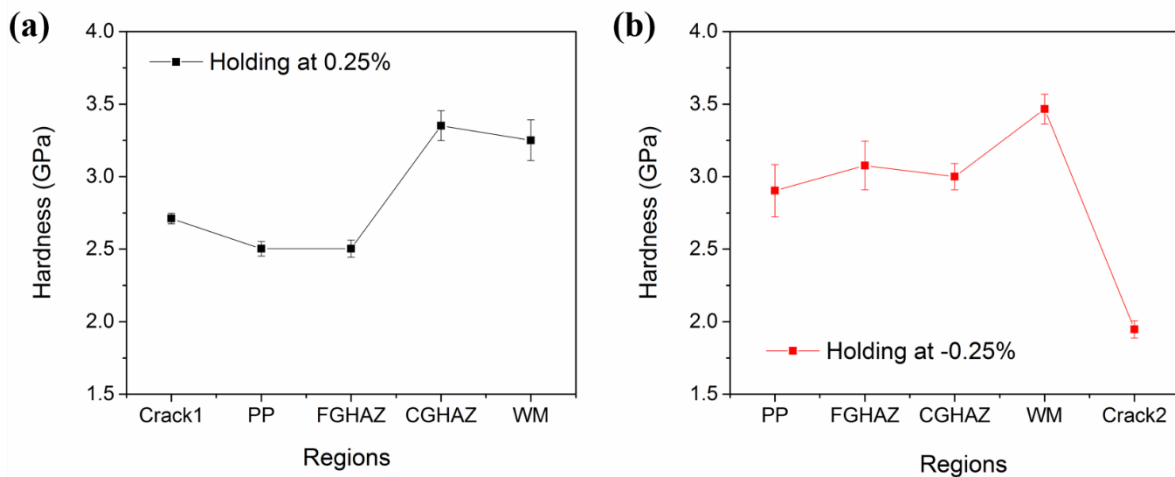

Figure 13 Comparison of measured hardness and elastic modulus near the fracture surface and in the PP, FGHAZ, CGHAZ and WM regions for specimens subject to either TH at 0.25% strain or CH at -0.25% strain: a) Hardness - TH b) Hardness - CH.
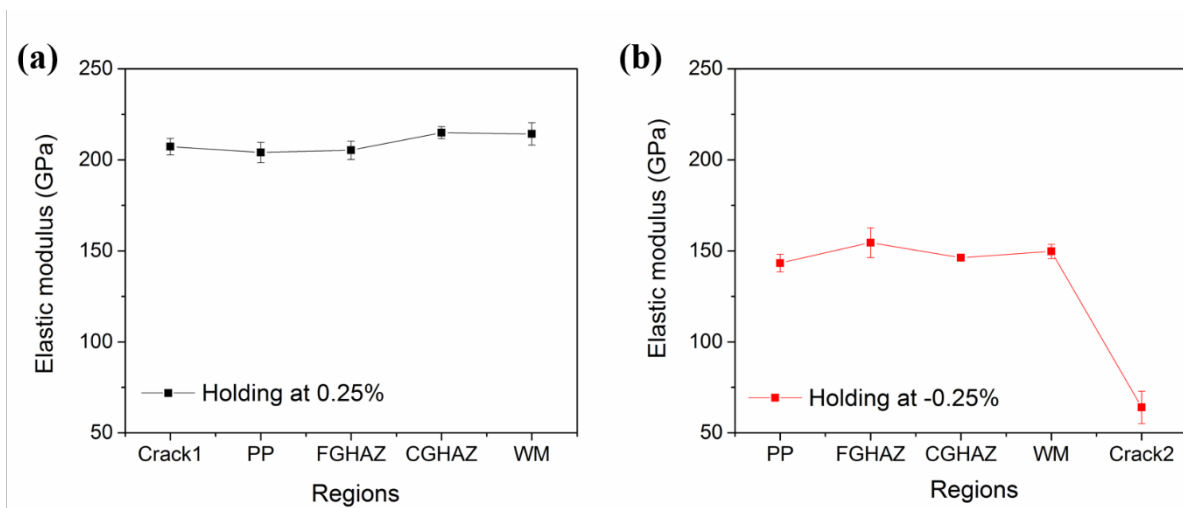

Figure 14 Comparison of measured hardness and elastic modulus near the fracture surface and in the PP, FGHAZ, CGHAZ and WM regions for specimens subject to either TH at 0.25% strain or CH at -0.25% strain: (a) Elastic modulus – TH and (b) Elastic modulus - CH.

To investigate the effect of compressive or tensile dwell strain on fracture mechanisms in the welded joint, the hardness and elastic modulus were measured near the fracture surface and in the four weld regions for the CH and TH specimens subject ±0.25% strain. In these two tests with a 300 s dwell period, a tensile strain led to cracking in the PP while a compressive strain initiated cracking in the WM. Figures 13(a) and 13(b) show the variation in hardness across the crack, and in the PP, FGHAZ, CGHAZ and WM regions for these TH and CH specimens. It is clear that the type of loading, i.e. tensile or compressive, has a very significant influence on the data. Considering the TH results, hardness is fairly uniform going from the PP across the crack and in the FGHAZ and it then increases sharply in the CGHAZ and WM. This is consistent with the location of the crack initiation being in the PP. In contrast, the CH data shows a fairly consistent level of hardness in the PP, FGHAZ and CGHAZ, and an increase in hardness in the WM. This is then followed by a significant drop near the crack, which had initiated in the WM. This is interpreted as indicating that crack initiation in the CH specimen reflects a strong component from cyclic softening and fatigue cracking, in agreement with the fracture surface data shown in Figure 9.

The elastic modulus data is presented in Figures 14(a) (TH specimen) and 14(b) (CH specimen) for all four microstructural zones and the near-fracture surface region. As would be expected the elastic modulus data follow the same trends seen in the hardness results.
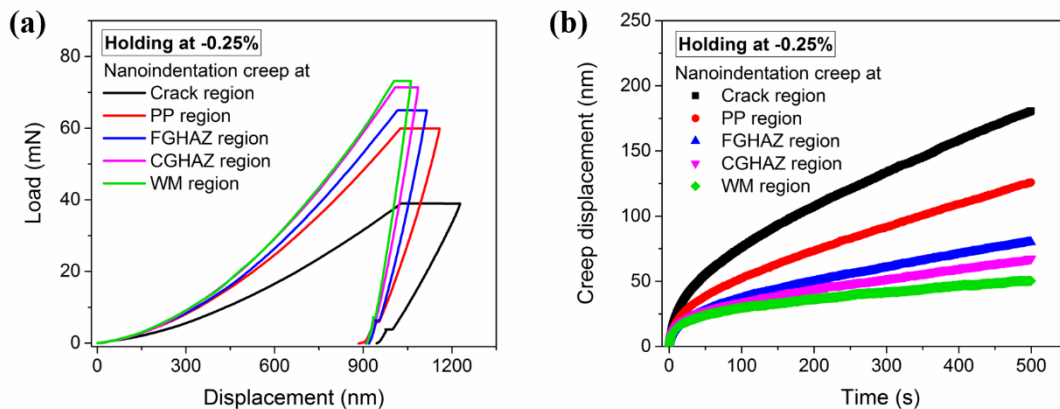
3.3 Nanoindentation creep

Figure 15(a) Representative load–displacement (*P-h*) curves measured during creep testing for the CH (300 s -0.25% strain) specimen; (b) Equivalent curves of creep displacement as a function of holding time for all microstructural regions.

Recalling that the specimens used in this work have all experienced prior CF cycling before the

nanoindentation creep testing was performed, typical load-indentation depth (*P-h*) curves measured during the nanoindentation creep for the four microstructural zones as well as near the crack are plotted in Figure 15(a) for the CH (-0.25%) specimen. The corresponding creep displacement measured from indentation depth during the CH dwell are given in Figure 15(b). To assist in interpretation of these curves, the origin of both holding time and creep displacement have been set to zero. The usual primary and secondary stages of creep deformation are clearly present. In the primary stage, creep deformation increases relatively quickly, while creep rate drops rapidly. In stage II creep, the deformation becomes almost linear with time and the creep rate is constant.
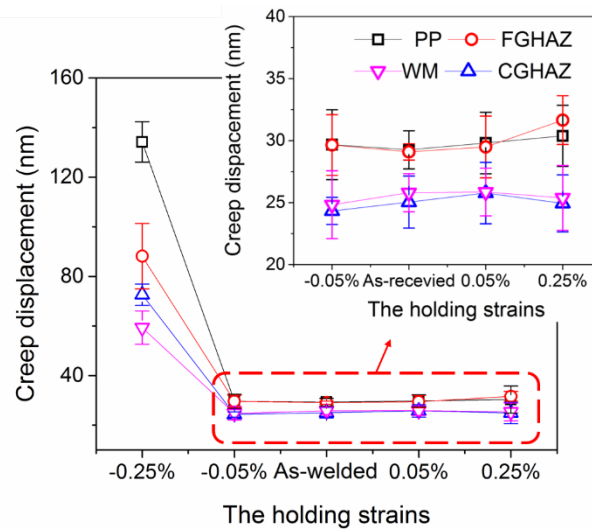

Figure 16 Comparison between creep displacement as a function of dwell strain for all microstructural regions for the as-welded and CF-tested specimens.

Figure 16 shows the variation in measured creep displacements for the PP, FGHAZ, CGHAZ and WM regions of as-welded and CF-tested specimens. In all cases, larger creep displacements were measured in the PP and FGHAZ regions, compared with the WM and CGHAZ zones and the creep displacement is relatively uniform with strain except for the case of dwell at -0.25% strain. This data again supports the interpretation of the images seen in Figure 8 and the data presented in Figure 12, in terms of the creep-fatigue mechanisms that are operative in the various weld zones.

Figures 17(a) and 17(b) replot the data in Figure 16 to show the variation in creep displacement across the five regions of interest for the TH (0.25% strain) and CH (-0.25% strain) specimens. It is clear that creep displacements under a 300 s dwell are much larger in the CH specimen. Creep displacement has an inverse form to the hardness data shown in Figure 13(a) and is maximized near the crack, reflecting the decrease seen in hardness at the crack site. Creep displacement is less variable across the various metallurgical zones in the TH specimen, supporting a greater fatigue component
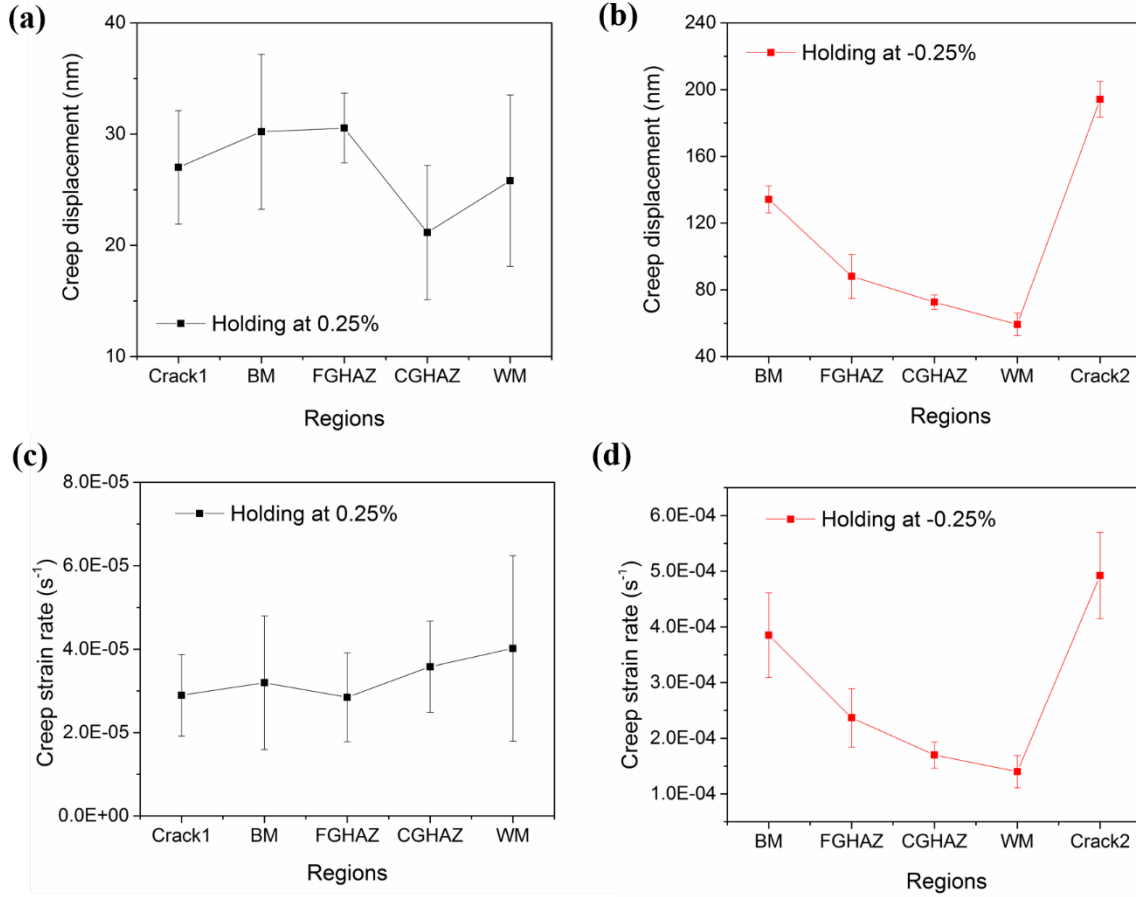
to the cracking observed in such tests.

Figure 17 Distributions of creep displacements across the crack, PP, FGHAZ, CGHAZ and WM regions for the (a) TH (0.25% holding) and (b) CH (-0.25% holding) specimens; distributions of creep strain rates across the five regions for (c) TH (0.25% holding) and (d) CH (-0.25% holding) specimens.

Steady-state creep strain rates across the five regions are more influenced by the local microstructure, decreasing from $\approx 4 \times 10^{-4}$ s^{-1} to $\approx 1.5 \times 10^{-4}$ s^{-1} in the WM, before increasing sharply near the crack to $\approx 5 \times 10^{-4}$ s^{-1}.

3.4 Strain rate sensitivity

Indentation creep has been widely applied to estimate strain rate sensitivity (SRS), and the technique can be extended to reveal information on the creep mechanism [38-39]. It is well-known that nanoindentation creep is dominated by mechanisms such as dislocation glide and climb, and grain boundary slide [39]. The SRS value (m) under the self-similar Berkovich indenter is given by [40]:

$$m \approx 2 \cdot \frac{\Delta \ln h}{\Delta \ln \left(t_{creep} \right)} = 2 \cdot \frac{\ln \left(h_2 / h_1 \right)}{\ln \left(t_2 / t_1 \right)} \tag{1}$$

Where t_1, t_2 were the time at beginning and ending of the holding stage, respectively. From the Eq. (1), the average value of m with a certain time interval [t_1, t_2] could be obtained. In this study, the creep deformation in the last 100 s of dwell period was used to estimate the local m for steady-state creep. The details of the method used to calculate the local SRS value m welded P92 steel joints was introduced in our previous study [29].
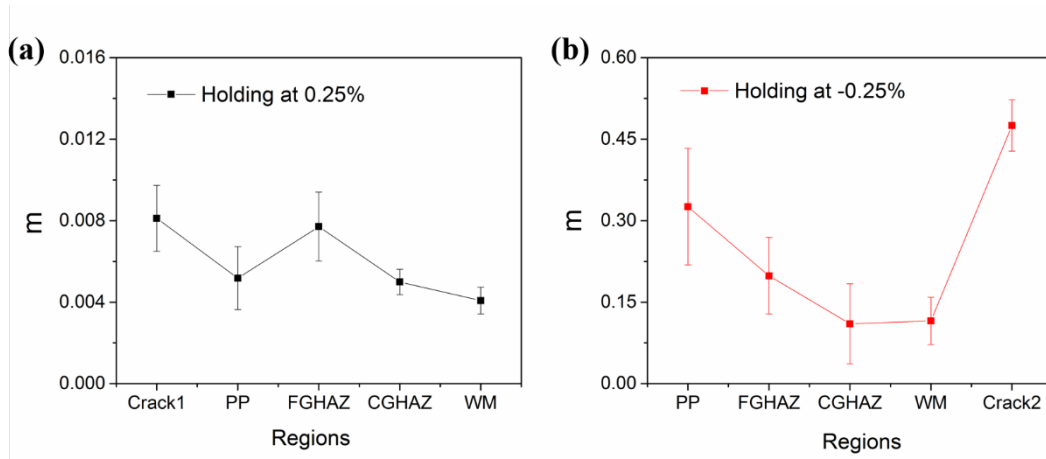

Figure 18. The local SRS (m) for the near-crack, PP, FGHAZ, CGHAZ and WM regions in the welded P92 steel joint for (a) TH (0.25%) and (b) CH (-0.25%) specimens.

Figures 18(a) and 18(b) show the values of m found using equation 1, in all weld zones for the TH (0.25% strain) and CH (-0.25% strain) specimens. For both specimens, the maximum value of m occurs in the crack region (0.008 for the TH specimen and 0.46 for the CH specimen), although the value in the TH FGHAZ zone is close to that measured near the crack. In the CH specimen, m is both higher and more variable than seen in the TH case. The m can be expressed as a function of dislocation density, which was proposed in our previous study [28]:

$$m = \frac{3\sqrt{3}k_b T}{a\mu b c V^*} \frac{1}{\sqrt{\rho}} \qquad (2)$$

Where ρ is the density of dislocations, V^* is the activation volume, k_b is Boltzmann's constant, T is the temperature in Kelvin, and a, μ, b, c are constants for a given material. Previous work on this alloy [28, 29] has reported that a decreased dislocation density and structural damage at grain boundaries lead to enhanced values of m, both of which are likely to be enhanced by long compressive dwell periods during creep-fatigue.

4. Discussion

4.1 Damage mechanisms during dwell periods in CF loading

The stress relaxation measured during dwell periods in strain-controlled CF tests, has been

illustrated in Figures 5 to Figure 7. Figure 5b and Figure 7 demonstrate that two stages were observed during the stress relaxation process; in the first stage, stress decreases sharply over the first 25-50 s and then remains approximately stable over the remaining dwell period. A recovery process of dislocation annihilation has been reported to occur during dwell periods, which would reduce dislocation density [41, 42]. However, several other investigations have indicated that a decreased dislocation density leads to a reduction in yield and tensile strength and a corresponding increase in cyclic softening after prior CF loading [43-45]. Figure 18 shows that the local strain rate sensitivity values, *m,* in the CH specimen were larger in all microstructural zones than in the TH specimen. This indicates that plastic deformation in the CH specimen is more severe and deleterious than in the TH specimen. Arising from this, cyclic lives were clearly shorter for the CH specimens at same strain amplitudes than observed in the TH specimens. The observed different stress relaxation behaviors for the TH and CH specimens is believed to be the main reason for this (see Figures 5b and 7). Wang et al [9] in work on P92 steel also found that periods of compressive dwell in CF tests had a more detrimental effect on fatigue life than periods of tensile dwell.

In the CF tests with either primarily elastic strain ranges or with primarily plastic strain ranges, the degree of stress relaxation (characterized by $\Delta\sigma$) seen in the stress-strain hysteresis loops was larger in the 30 s dwell period than that observed in the 300 s dwell (see Figure 8), although the difference was more marked in the TH tests, compared with the CH data. Furthermore, the value of $|\sigma_{steady}|$ that characterizes steady-state creep, was significantly higher in the TH tests with a 300 s dwell, compared with the 30 s dwell, while the values in the CH tests were very close for both dwell periods.

Creep damage accumulates during dwell periods, and creep deformation is facilitated under higher stress levels [8, 9]. Creep damage would therefore be reduced due to the decrease values of $|\sigma_{steady}|$ during CF in the TH specimens. In contrast, an enhanced accumulation of creep damage would produce more numerous intergranular creep voids (microcracks) seen in the fractographs for the CH specimen (Figure 10). Creep voids (microcracks) assist cracking [42] and accelerate the interactive creep-fatigue damage. Hence shorter cyclic lifetimes were found with the CH specimens rather than in the TH specimens.

4.2 Local room-temperature creep behavior after CF loadings

The CF process facilitates the initiation of creep microvoids, especially near the tip of a crack, due to large local stress concentrations and plastic deformation [45]. Nondestructive detection of these internal microvoids is difficult, even using ultrasonic techniques, which have a minimum detection size of ≈20 μm. An indirect method of characterizing the presence of such defects is required.

The nanoindentation data for elastic modulus presented in Figure 12(b) indicates a steep

reduction in the room-temperature elastic modulus for CF specimens subject dwell in the plastic strain range (-0.25%). The room-temperature elastic modulus is known to be more sensitive to alloy composition rather than to microstructure [46-48]. The chemical composition of P92 steel will not be altered during exposure to high-temperature (650°C) deformation, and the elastic modulus has been reported to be inversely proportional to pore volume fraction for a number of materials [e.g. 49, 50]. In CF specimens, creep microvoids are nucleated during testing and form nano- to micro-scale defects at grain boundaries. These microvoids/defects increase the pore volume fraction in the nanoindentation test area. It can therefore be deduced that the reduced room-temperature elastic modulus observed in all microstructural regions in the test at strain of -0.25% are evidence of the existence of creep microvoids in CF specimen.

Under long-term creep loading, welded joints in Cr-Mo steel have been reported to fracture in the PP and FGHAZ regions by a number of other workers [18, 51-52]. Figure 16 shows that increased creep displacements were measured in the PP and FGHAZ regions in all the CF specimens. In these two regions, the reduced resistance to plastic strain would induce intergranular creep voids (microcracks) to link together, forming larger creep voids or cracks and eventually leading to rupture. The initiation of intergranular creep voids is likely to be facilitated in these two regions due to high grain boundary density [18]. It is therefore clear that the PP and FGHAZ regions are most vulnerable to creep damage during long term high-temperature service of welded joints in Cr-Mo steel.

It is also the case that the present work has added further evidence that enhanced creep deformation occurs during periods of compressive dwell, compared with tensile dwell (Figure 16).

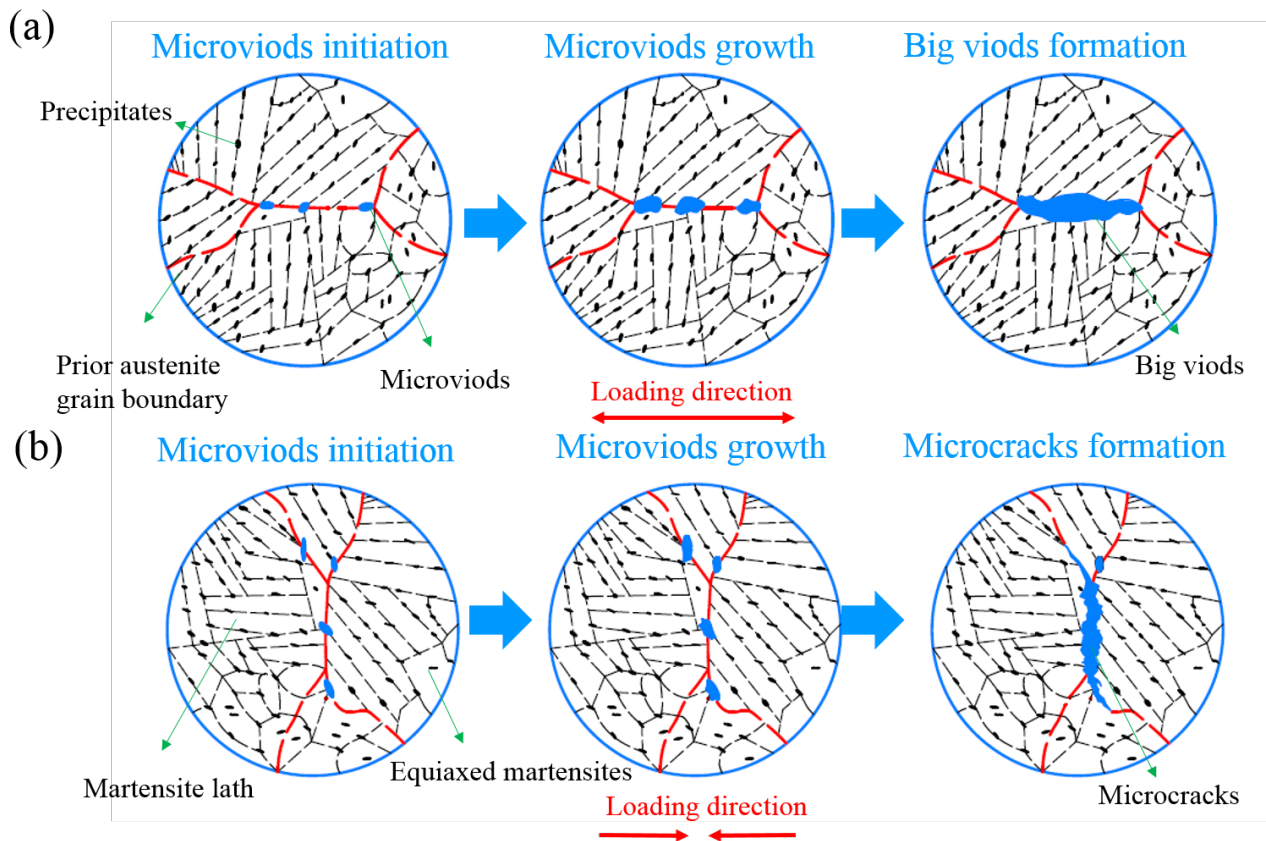**4.3 Fracture mechanisms under TH and CH loading**

Figure 19 Schematic representation of creep-fatigue fracture mechanisms for welded joints in P92 steel under (a) tensile dwell at 0.25% strain and (b) compressive dwell at -0.25% strain.

Figure 19 depicts the fracture mechanisms in a similar schematic diagram to that given in reference [18] The fracture mechanisms observed in the TH specimens are schematically illustrated in Figure 19(a). Microvoids have been reported to initiate at precipitate-matrix boundaries due to their local high stress concentration, and are also nucleated at PAGBs or block boundaries [18]. These creep voids generally converge into larger voids, which have been clearly observed in TH specimens, see Figures 10(c) and 10(d). The major axis of these larger voids is vertical to the fracture surface. The martensitic laths transform to equiaxed martensite in the HAZ due to recovery during post-welding heat treatment, as shown in in our previous study [30], and equiaxed martensite is less sensitive to fatigue damage accumulation [18]. Since the PP region adjacent to the HAZ retains a higher proportion of martensitic lath structures, it would experience a greater level of microstructural recovery during creep testing, leading to accelerated CF damage accumulation, as noted in reference [18]. Creep-fatigue fracture therefore eventually occurs in the PP region in TH specimens.

The development of fracture in the CH specimens is illustrated in Figure 19(b). The creep-fatigue fracture initiation sites in the CH specimen (under a dwell at -0.25% strain) shift from the PP to the WM region (Figure 3(b)), and a remarkable reduction in cyclic life is observed. Figure 19(b)

illustrates that microvoids also occur at grain boundaries, and that they tend to initiate from PAGBs or block boundaries and propagate along the boundaries. The direction of propsagation and eventual convergence of these voids reflects the principal stress in the resultant stress system arising from the applied load. Figures 10(a) and 10(b) show that these voids eventually converged to become microcracks. As a consequence of this, more severe fatigue damage accumulates, leading to a significant reduction in the CF life of the welded joint. With increasing strain amplitudes, the degree of fatigue damage gradually increases in the overall creep-fatigue process.

5. Conclusions

This paper presents a study of the nanoindentation creep behavior and fracture mechanism of as-welded, CF-tested P92 steel welds with tensile or compressive holdings at different amplitudes. The local hardness, modulus, creep deformations were obtained in the PP, FGHAZ, CGHAZ and WM regions for all specimens, as well as crack regions of the plastic-holdings ($\pm$0.25% strain) specimens. The SRS (*m*) were estimated for all regions from the nanoindentation results. The following conclusions can be drawn:

1. For P92 steel welded joint, the pronounced cyclic softening phenomenon is occurred under plastic amplitudes. The cyclic lifetimes were more severely reduced under long-term compressive holding periods than under tensile holds at same strain amplitudes. Furthermore, the reduced CF lives were mainly caused higher steady stress levels $\left|\sigma_{\text{steady}}\right|$ for the CH specimens, which was compared with the TH specimen at same amplitude.

2. Compared with the as-welded specimen, the hardness, modulus, creep resistance in the PP, FGHAZ, CGHAZ and WM regions were stable under prior CF loadings with elastic amplitude. However, these material properties were significantly reduced after plastic-amplitude CF loadings, especially with compressive dwell. The remarkable decreased elastic modulus could be resulted by the nucleation of numerous tiny creep voids. In addition, the CF loading with compressive dwell facilitates these tiny creep voids, which result in the degradation of room-temperature creep resistance.

3. All the specimens were fractured in the PP region except the CH (-0.25% holding) specimen, which was fractured in the WM region. In comparison to the TH (0.25% holding) specimen, the hardness, elastic modulus, creep resistance in the crack region were clearly reduced for the CH specimen.

4. The tiny creep voids or nanoscale defects converged to form the big creep voids for the TH specimen, while these voids extended to form microcracks for the CH specimen. Since the same directions of fatigue crack propagation and these tiny void or nanoscale defects converging, the severer fatigue damage accumulation is induced. It could be the main reason that significantly

reduced the CF life for the CH specimens.

Declaration of Competing Interest

We declare that we have no conflict of interest.

Acknowledgements

References

[1] J. Ni, X. Zhuang, M.A. Wahab. Review on the prediction of residual stress in welded s teel components. Comput. Mater. Con. 62 (2020) 495–523. DOI: 10.32604/cmc.2020.08448.

[2] J. Ni, J.V. Voorde, J. Antonissen, M.A. Wahab. Dependency of phase transformation on the prior austenite grain size and its influence on welding residual stress of S700 steel. Weld World. 62 (2018) 699–712. DOI: 10.1007/s40194-018-0575-9.

[3] J. Ni, X.W. Wang, J.M. Gong, M.A. Wahab. Thermal, metallurgical and mechanical analysis of circumferentially multi-pass welded P92 steel pipes. Int. J. Press. Vessel. Pip. 165 (2018) 164–175. DOI: 10.1016/j.ijpvp.2018.06.009.

[4] S.T. Tu, P. Segle, JM. Gong. Creep damage and fracture of weldments at high temperature. Int. J. Press. Vessel. Pip. 81 (2004) 199–209. DOI: 10.1016/j.ijpvp.2003.11.010.

[5] S.J. Guo, R.Z. Wang, H.F. Chen, F.Z. Xuan. A comparative study on the cyclic plasticity and fatigue failure behavior of different subzones in CrNiMoV steel welded joint. Int. J. Mech. Sci.150 (2019) 66–78. DOI: 10.1016/j.ijmecsci.2018.10.026.

[6] V. Gaffard, A.F. Gourgues-Lorenzon, J. Besson. High temperature creep flow and damage properties of 9Cr1MoNbV steels: base metal and weldment. Nucl. Eng. Des. 235 (2005) 2547–2562. DOI: 10.1016/j.nucengdes.2005.07.001.

[7] L. Chang, X. Li, J.B. Wen, Zhang, et al. Thermal-mechanical fatigue behaviour and life prediction of P92 steel, including average temperature and dwell effects. J. Mater. Res. Technol. 9 (2020) 819–837. DOI: 10.1016/j.jmrt.2019.11.022.

[8] X.C. Zhang, S.T. Tu, F.Z. Xuan. Creep-fatigue endurance of 304 stainless steels. Theor. Appl. Fract. Mech. 71 (2014) 51–66. DOI: 10.1016/j.tafmec.2014.05.001.

[9] X.W. Wang, W. Zhang, T.Y. Zhang, et al. A new empirical life prediction model for 9–12% Cr steels under low cycle fatigue and creep fatigue interaction loadings. Metals. 9 (2019) 183. DOI: 10.3390/met9020183.

[10] X.W. Wang, W. Zhang, J.M. Gong, et al. Low cycle fatigue and creep fatigue interaction behavior of 9Cr-0.5 Mo-1.8WV-Nb heat-resistant steel at high temperature. J. Nucl. Mater. 505 (2018) 73–84. DOI: 10.1016/j.ijfatigue.2015.09.00.

[11] T.H. Hyde, M. Saber, W. Sun. Testing and modelling of creep crack growth in compact tension specimens from a P91 weld at 650 C. Eng. Fract. Mech. 77 (2010) 2946–2957. DOI: 10.1016/j.engfracmech.2010.03.043.

[12] K. Laha, K.S. Chandravathi, K.B.S Rao, S.L. Mannan, D.H. Sastry. An assessment of creep deformation and fracture behavior of 2.25 Cr-1Mo similar and dissimilar weld joints. Metall. Mater. Trans. A. 32 (2001) 115–124. DOI: 10.1007/s11661-001-0107-9.

[13] S.T. Tu. Creep behavior of crack near bi-material interface characterized by integral parameters. Theor. Appl. Fract. Mech. 38 (2002) 203–209. DOI: 10.1016/S0167-8442(02)00088-5.

[14] A. Sarkar, V.D. Vijayanand, P. Parameswaran, et al. Influence of prior fatigue cycling on creep behavior of reduced activation ferritic-martensitic steel. Metall. Mater. Trans. A. 45 (2014) 3023–3035. DOI: 10.1007/s11661-014-2237-x.

[15] L. Binda, S.R. Holdsworth, E. Mazza. Influence of prior cyclic deformation on creep properties of 1CrMoV. Mater. High. Temp. 27 (2010) 21–27. DOI: 10.3184/096034009X12602928724673.

[16] T.D. Joseph, D. McLennon, M.W. Spindler, et al. The effect of prior cyclic loading variables on the creep behavior of ex-service Type 316H stainless steel. Mater. High. Temp. 30 (2013) 156–160. DOI: 10.3184/096034013X13717271415898.

[17] T. Mayama, K. Sasaki. Investigation of subsequent viscoplastic deformation of austenitic stainless steel subjected to cyclic preloading. Int. J. Plast. 22 (2006) 374–390. DOI: 10.1016/j.ijplas.2005.03.008.

[18] W. Zhang, T. Zhang, X. Wang, et al. Remaining creep properties and fracture behavior of P92 steel welded joint under prior low cycle fatigue loading. J. Mater. Res. Technol. 9 (2020) 7887-7899. DOI: 10.1016/j.jmrt.2020.05.078.

[19] B. Fournier, M. Sauzay, C. Caes, et al. Creep-fatigue-oxidation interactions in a 9Cr-1Mo martensitic steel. Part II: Effect of compressive holding period on fatigue lifetime. Int. J. Fatigue. 30 (2007) 663-676.

[20] N. Gao, M. W. Brown, K. J. Miller, et al. An investigation of crack growth behaviour under creep-fatigue condition. Mater. Sci. Eng. A. 410 (2005) 67-71. DOI: 10.1016/j.msea.2005.08.076.

[21] Y. Ma, G.J. Peng, D.H. Wen, et al. Nanoindentation creep behavior in a CoCrFeCuNi high-entropy alloy film with two different structure states. Mater. Sci. Eng. A. 621 (2015) 111-117. DOI: 10.1016/j.msea.2014.10.065.

[22] Y. L. Yu, Y. Ma, X. W. Huang, et al, Annealing effect on the structure relaxation and mechanical properties of a Polytetrafluoroethylene film by RF-magnetron sputtering. Surf. Coat. Tech. 405 (2021) 126591. DOI: 10.1016/j.surfcoat.2020.126591.

[23] Y. Ma, G.J. Peng, Y.H. Feng, et al. Nanoindentation investigation on the creep mechanism in metallic glassy films. Mater. Sci. Eng. A. 651 (2016) 548-555. DOI: 10.1016/j.msea.2015.11.014.

[24] Y. Ma, X. W. Huang, W, Hang, et al. Nanoindentation size effect on stochastic behavior of incipient plasticity in a LiTaO3 single crystal. Eng. Fract. Mech., 226 (2020), 106877. DOI: 10.1016/j.engfracmech.2020.106877.

[25] Y. L. Yu, X.Q. Xu, C.D. Lu, et al. Investigation on the microstructural and mechanical

properties of a Polytetrafluoroethylene thin film by Radio Frequency magnetron sputtering. Thin Solid Films. 712 (2020) 138302. DOI: 10.3390/met9050613.

[26] Y.X. Song, X.W. Huang, Z.L. Gao, et al. Nanoindentation creep behavior of RPV's weld joint at room temperature. Mech. Time-Depend. Mater. 24 (2020) 253-263. DOI: 10.1007/s11043-019-09419-y.

[27] N. Komai, F. Masuyama. Microstructural Degradation of the HAZ in 11Cr-0.4Mo-2W-V-Nb-Cu Steel (P122) during Creep. ISIJ Int. 42 (2002): 1364-1370.

[28] Z.L. Gao, Y.X. Song, Z.X. Pan, J.N. Chen, Y. Ma, Nanoindentation investigation on the creep behavior of P92 steel weld joint after creep-fatigue loading. Int. J. Fatigue. 134 (2020) 105506. DOI: 10.1016/j.ijfatigue.2020.105506.

[29] Y.X. Song, F.R. Qin, J. N. Chen, et al. On the microstructural evolution and room-temperature creep behavior of 9%Cr steel weld joint under prior creep-fatigue interaction. Fatigue. Fract. Eng. Mater. Struct. 44 (2021) 444-460. DOI: 10.1111/ffe.13370.

[30] Y.X. Song, Z. X. Pan, J. N. Chen, et al. The effect of prior creep-fatigue on strain rate sensitivity in a P92 welded joint. J. Mater. Sci. 56 (2021) 7111-7128. DOI: 10.1007/s10853-020-05665-5.

[31] L. Susmel, D. Taylor. Two methods for predicting the multiaxial fatigue limits of sharp notches. Fatigue. Fract. Eng. Mater. Struct. 26 (2003) 821-833. DOI: 10.1046/j.1460-2695.2003.00683.x.

[32] L. Zhao, L. Xu, Y. Han, et al. Analysis on stress-strain behavior and life prediction of P92 steel under creep-fatigue interaction conditions. Fatigue. Fract. Eng. Mater. Struct. 43 (2020) 2731–2743. DOI: 10.1111/ffe.13341.

[33] R. Z. Wang, X. C. Zhang, S. T. Tu, et al. Zhang. A modified strain energy density exhaustion model for creep–fatigue life prediction. Int. J. Fatigue. 90 (2016) 12-22. DOI: 10.1016/j.ijfatigue.2016.03.005.

[34] R. Z. Wang, X. C. Zhang, J. G. Gong, et al. Creep-fatigue life prediction and interaction diagram in nickel-based GH4169 super alloy at 650 ℃ based on cycle-by-cycle concept. Int. J. Fatigue. 97 (2017) 114-123. DOI: 10.1016/j.ijfatigue.2016.11.021.

[35] W. Ostergren. A damage function and associated failure equations for predicting hold time and frequency effects in elevated temperature, low cycle fatigue. J. Test. Eval. 4 (1976) 327–339.

[36] V. Shankar, M. Valsan, K. B. S. Rao, et al. Low cycle fatigue behavior and microstructural evolution of modified 9Cr–1Mo ferritic steel. Mater. Sci. Eng. A. 437 (2006) 413–422.

[37] M. Yaguchi, M. Yamamoto, T. Ogata. A viscoplastic constitutive model for nickelbase superalloy, part 1: kinematic hardening rule of anisotropic dynamic recovery. Int. J. Plast. 18 (2002)

1083–1109.

[38] K.L. Johnson. Contact Mechanics.UK: Cambridge University Press; 1987.

[39] W.B. Li, J.L. Henshall, R.M. Hooper, et al. The mechanisms of indentation creep. Acta. Metal. Mater. 39 (1999) 3099–3110. DOI: 10.1016/0956-7151(91)90043-Z.

[40] Q. Wei, S. Cheng, K.T. Ramesh, E. Ma. Effect of nanocrystalline and ultrafine grain sizes on the strain rate sensitivity and activation volume: fcc versus bcc metals. Mater. Sci. Eng. A. 381 (2004) 71-79. DOI: 10.1016/j.msea.2004.03.064.

[41]T. Watanabe, M. Tabuchi, M. Yamazaki,et al. Creep damage evaluation of 9Cr–1Mo–V–Nb steel welded joints showing Type IV fracture. Int. J. Pres. Ves. Pip. 83 (2006) 63-71. DOI: 10.1016/j.ijpvp.2005.09.004.

[42]K .Gopinath, R.K. Gupta, et al. Designing P92 grade martensitic steel header pipes against creep–fatigue interaction loading condition: Damage micromechanisms. Mater. Des. 86 (2015) 411–420. DOI: 10.1016/j.matdes.2015.07.107.

[43]K. Takasawa, R. Ikeda, N. Ishikawa, et al. Effects of grain size and dislocation density on the susceptibility to high-pressure hydrogen environment embrittlement of high-strength low-alloy steels. Int. J. Hydrogen. Energ. 37 (2012) 2669–2675. DOI: 10.1016/j.ijhydene.2011.10.099.

[44]C.G. Panait, A. Zielińska-Lipiec, T. Koziel, et al Evolution of dislocation density, size of subgrains and MX-type precipitates in a P91 steel during creep and during thermal ageing at 600 C for more than 100000 h. Mater. Sci. Eng. A. 527 (2010) 4062–4069. DOI: 10.1016/j.msea.2010.03.010.

[45]W. Zhang, X.W. Wang, H.F. Cheng, et al. Evaluation of the effect of various prior creep-fatigue interaction damages on subsequent tensile and creep properties of 9%Cr steel. Int. J. Fatigue. 125 (2010) 440-453. DOI: 10.1016/j.ijfatigue.2019.04.018.

[46]D. Zhao, X.H. Chen, Y. Yuan, et al. Development of a novel Mg–Y–Zn–Al–Li alloy with high elastic modulus and damping capacity. Mater. Sci. Eng. A. 790 (2020) 13944. DOI: https://doi.org/10.1016/j.msea.

[47]B. Liu, X.B. Zhang, Z.C. Huang, et al. Microstructure and properties of a novel ultra-high strength, high elasticity and high plasticity Cu–20Ni–20Mn-0.3Nb-0.3Cr-0.1Zr alloy. J Alloys Compd. (2020) 157402. DOI: https://doi.org/10.1016/j.jallcom.

[48]Y.C. Zhang, X.T. Yu, W.C. Jiang, et al. Elastic modulus and hardness characterization for microregion of Inconel 625/BNi-2 vacuum brazed joint by high temperature nanoindentation. Vacuum. 187 (2020) 109582.DOI: https://doi.org/10.1016/j.vacuum.

[49]J. Werner, C.G. Aneziris, S. Schafföner. Influence of porosity on Young's modulus of carbon-bonded alumina from room temperature up to 1450 °C. Ceram. Int. 40 (2014) 14439-14445.

DOI: 10.1016/j.ceramint.2014.07.013.

[50]E. Garlea, H. Choo, C.C. Sluss, et al. Variation of elastic mechanical properties with texture, porosity, and defect characteristics in laser powder bed fusion 316L stainless steel. Mater. Sci. Eng. A. 763 (2019) 138032. DOI: 10.1016/j.msea.2019.138032.

[51]M. Matsui, M. Tabuchi, T. Watanabe, et al. Degradation of creep strength in welded joint of 9% Cr steel. ISIJ. Int. 41 (2001) 126–130. DOI: 10.2355/isijinternational.41.Suppl_S126.

[52]S.K. Albert, M. Matsui, T. Watanabe, et al. Variation in the type IV cracking behavior of a high Cr steel weld with post weld heat treatment. Int. J. Press. Vessel. Piping. 80 (2003) 405–413. DOI: 10.1016/S0308-0161(03)00072-3.